Effects of fast X-Ray cone-beam tomographic measurement on dimensional metrology

Charalambos Rossides[1], Hossein Towsyfyan[2], Ander Biguri[3], Hans Deyhle[4], Reuben Lindroos[5], Mark Mavrogordato[1], Richard Boardman[1], Wenjuan Sun[6], Thomas Blumensath[1,2]

[1] μ-VIS X-Ray Imaging Centre, University of Southampton, Southampton, SO17 1BJ

[2] Institute of Sound and Vibration Research, University of Southampton, Southampton, SO17 1BJ

[3] Department of Applied Mathematics and Theoretical Physics, University of Cambridge, Cambridge, CB3 0WA

[4] Diamond Light Source Ltd, Harwell Science & Innovation Campus, Didcot, OX11 0DE

[5] Department of Computer Science, The University of Bath, Bath, BA2 7AY

[6] National Physical Laboratory, Hampton Road, Teddington, TW11 0LW

E-mail: thomas.blumensath@soton.ac.uk

Abstract

X-ray computed tomography (XCT) is increasingly used for dimensional metrology, where it can offer accurate measurements of internal features that are not accessible with other techniques. However, XCT scanning can be relatively slow, which often prevents routine uptake for many applications. This paper explores the feasibility of improving the speed of XCT measurements whilst maintaining the quality of the dimensional measurements derived from reconstructed volumes. In particular, we compare two approaches to fast XCT acquisition, the use of fewer XCT projections as well as the use of shortened x-ray exposure times for each projection. The study shows that the additional Poisson noise produced by reducing the exposure for each projection has significantly less impact on dimensional measurements compared to the artefacts associated with strategies that take fewer projection images, leading to about half the measurement error variability. Advanced reconstruction algorithms such as the conjugate gradient least squares method or total variation constrained approaches, are shown to allow further improvements in measurement speed, though this can come at the cost of increased measurement bias (e.g. 2.8 % increase in relative error in one example) and variance (e.g. 25 % in the same example).

1. Introduction

Coordinate measuring machines (CMM), which are typically used in dimensional measurement, physically drag a contact probe across the surface [1], [2]. These measurements can thus be greatly affected by the texture of the surface (the mechanical filtering effect), which can be an issue in additive manufacturing [3], where the structure itself might be distorted through a combination of different contact mechanisms [4], [5]. Tactile and optical techniques furthermore do not allow the characterization of internal structures found in many complex additive manufacturing geometries if these do not permit line-of-sight access [3].

Over the past few years, x-ray computed tomography (XCT) [6] has emerged as an attractive alternative to tactile or optical CMM and has increasingly been used in a broad range of applications in manufacturing and production engineering [7], [8], additive manufacturing process [9], [10] or production integrated inspection of components [11], [12], [13]. It has been demonstrated that XCT is able to produce
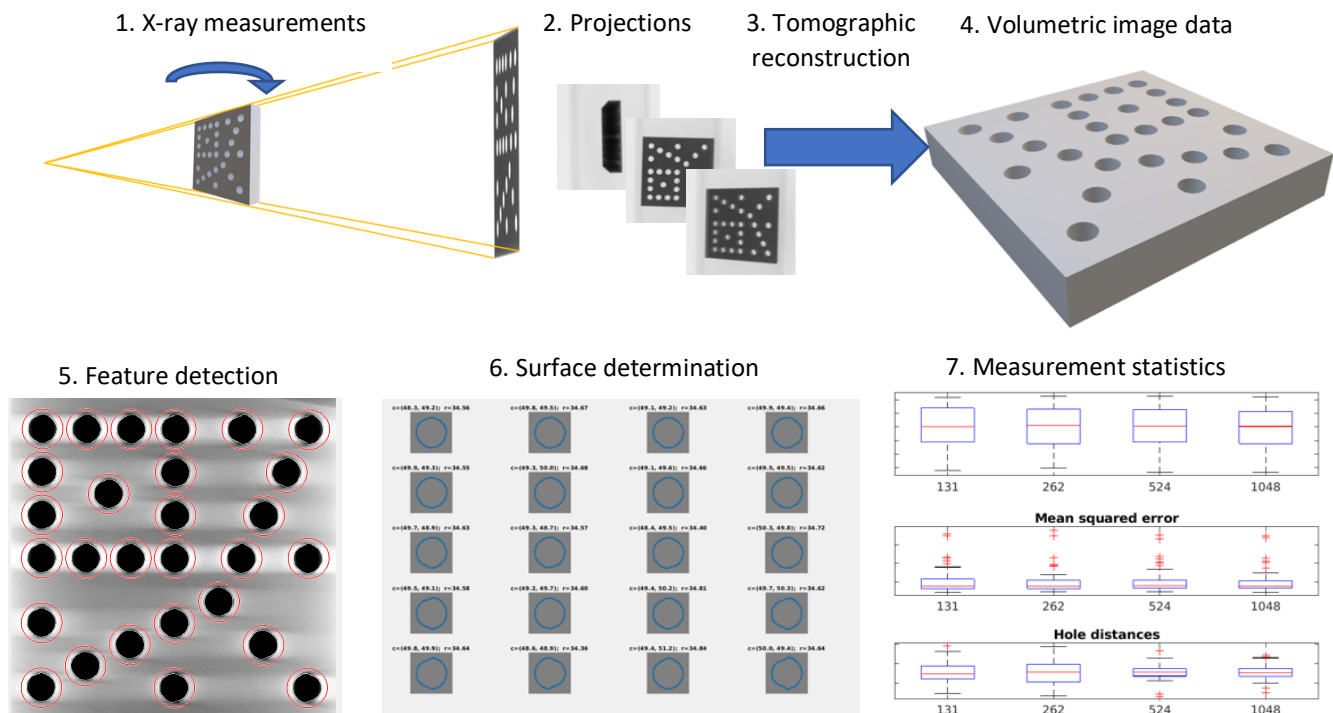
Figure 1: Workflow for the XCT metrology process.

results comparable to those of CMMs and optical inspection systems [14] [15] [2], even though it can still suffer from several sources of measurement error [16], [17]. XCT metrology and quality control [8], [18], [19] has nevertheless undergone a paradigm shift toward holistic, high-resolution measurements applicable to in-line manufacturing applications where it offers several advantages, including non-destructive evaluation of both internal (e.g. non-accessible) features [20]) as well as external geometrical features and surface texture characterization with micrometre accuracy [21], [22]. XCT has furthermore the potential to verify parts in assembled states, allowing the detection of manufacturing and assembly induced imperfections, provides simultaneous dimensional and material quality control, and provides complete and high-density point clouds in a relatively short time, all of which are typically not provided by other measurement methods.

To estimate feature dimensions using XCT, several steps are required: tomographic scanning; volumetric image reconstruction [23]; image segmentation [24]; surface determination [25] and dimensional evaluation [16]. This workflow is summarised in Figure 1.

Image reconstruction in cone beam CT (the most common form of XCT in industrial settings) is typically done using the Feldkamp, Davis, Kress (FDK) algorithm [23], which is relatively fast and works well in settings where we have enough x-ray transmission through the object (and thus low Poisson noise in each projection) and where we can collect x-

ray projections at sufficiently closely spaced angles to satisfy the tomographic sampling theorem [26]. For reconstruction with higher levels of Poisson noise or from limited projections, *iterative optimisation methods* are often suggested [27], [28]. These methods are significantly slower than FDK reconstruction, which significantly increases computer hardware requirements as well as reconstruction time. Recent advances in specialised GPU accelerated XCT reconstruction software now enable the use of these techniques also for cone-beam tomographic reconstruction of three dimensional images of realistic size [29], though reconstruction of large volumes can still take several hours [29], restricting their use for inline inspection. Iterative optimisation methods include the conjugate gradient least squares algorithm (CGLS) [30] [31] [32], which optimises a least squares objective, though due to ill-conditioning of the XCT inverse problem, regularised methods, such as the fast iterative shrinkage/thresholding algorithm (FISTA) [33] are often preferable. Whilst different approaches to regularisation have been suggested (including early stopping of the CGLS algorithm, which provides implicit regularisation), image smoothness assumptions such as those enforced by the Total Variation constraint [34] are often preferred, as they provide explicit specification and control of image smoothness conditions.

Once the XCT volumetric image has been reconstructed, dimensional information can be extracted by determination object boundaries. Surface determination is realised by various techniques such as assigning or estimating an
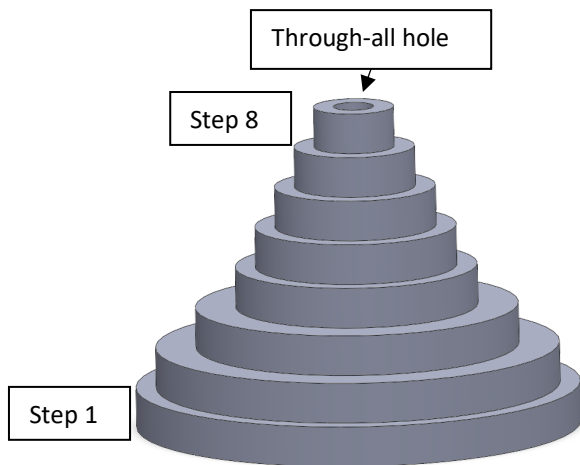
Figure 2: A schematic lay-out of the calibrated cylinder-stack sample. The sample is manufactured out of aluminium and consists of 8 equal height steps. The overall height is 160 mm. The sample also has a 20 mm central through hole. Measured diameters along the centre of each step are given in Table 1.

Figure 3: A schematic lay-out of the hole-plate sample.

optimal threshold grey value for edge voxels [25], [35], [36], or interpolation between voxel grey values [37]. Often, parametric curves are then fitted to describe the boundary surface. Once a surface description is parameterised, dimensional measurements can be obtained in conjunction with calibration data [2] [38]. Despite the rapidly increasing number of applications of dimensional CT metrology in industrial settings [8] [39] [7] [41] [41], uptake of this technology remains restricted by the relatively slow scan speed, which often makes the routine inspection of components in a production line setting infeasible [19] [42]).

There are two standard approaches available to increase scan speed in XCT: 1) reducing the number of projection images acquired [43] and 2) reducing the x-ray exposure time for each image. When reducing the number of projection images, FDK based reconstruction leads to images with significant artefacts, which in turn often prevent accurate surface determination, whilst decreased exposure times increases image noise and is thus likely to also increase metrological measurement uncertainty.

In this paper we evaluate performance of two different approaches to increase XCT measurement speed for dimensional metrology. We vary the number of projections (sparse data) and the x-ray exposure times (noisy data). We are particularly interested in the degradation of measurement performance in these settings and on the mitigating effects achievable when replacing the standard FDK algorithm with iterative reconstruction algorithms such as the conjugate gradient method (CGLS) and the Total Variation constrained FISTA algorithm (FISTA-TV).
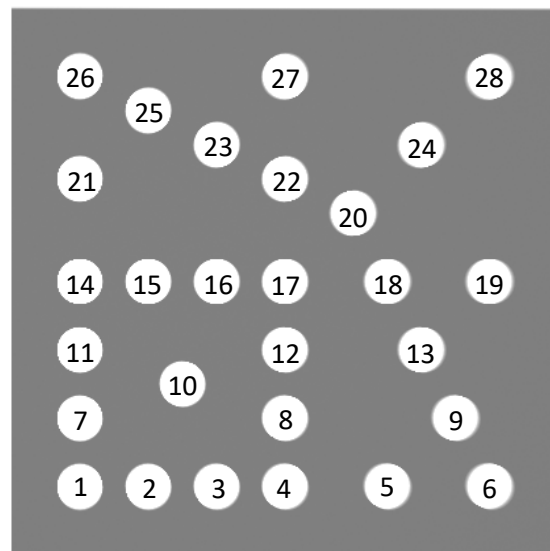
2. Materials and methods

We designed a set of experiments and simulations to investigate the performance of the three candidate reconstruction algorithms (FDK, CGLS and FISTA-TV) on fast tomographic acquisition data.

As the sample geometry is application dependent, we investigate two extreme cases i) a sample with cylindrical symmetry that provides consistent beam path length at all radiographic angles, and ii) a sample with a flat panel geometry that was mounted so that x-ray paths lengths varied greatly at different angles. Both samples were metal, which introduced additional non-linear attenuation effects known as beam hardening, which are often encountered in inspection settings. The samples were scanned twice using our in-house custom built XCT scanner. One slow scan minimised noise and blurring whilst a fast scan had a much higher noise level.

The low noise (long exposure) scan data was used to generate additional data-sets. By adding additional Poisson noise, data with intermediate noise levels was generated, whilst by removing a subset of the projection images from the data, limited projection acquisitions were generated. The different data-sets were then reconstructed with the FDK, CGLS and FISTA-TV reconstruction algorithms (see section 2.4). Surfaces were fitted to different structures in each volumetric image from which metrological measurement points could be extracted and compared with dimensional information measured using co-ordinate measurement machines (see section 2.5). As each sample has several features, this gave us a wide range of metrological measurements for each of the conditions of interest, whilst fixing many of the aspects of the experiment (such as sample shape and material) that are also known to influence

metrological performance, but whose variation would here hide the influence of the different imaging approaches and reconstruction algorithms on measurement accuracy and precision.

2.1 Sample designs and dimensions

The step-cylinder and CMM reference measurements were provided by the Swiss Federal Laboratories for Materials Science and Technology (EMPA) [44]. This 160 mm heigh aluminium sample features 8 concentric cylindrical steps of equal height but with different diameters and a concentric through-all hole as shown in Fig. 2 and Table 1.

Table 1: The dimensions of the cylinder-stack sample measured with a CMM device.

Feature	Diameter/mm	Cylindricity/mm
Inside top	20.0145	0.0070
step8	40.0074	0.0059
step7	59.9989	0.0037
step6	79.9922	0.0047
step5	99.9872	0.0039
step4	119.9832	0.0034
step3	159.9824	0.0061
step2	199.9851	0.0084
step1	220.0319	0.0200
Inside bottom	20.0337	0.0105

Table 2: Example dimensions of the hole-plate sample measured with a CMM device (average over three repeat measurements, all measurements were available but are omitted here for compactness).

Hole number	Diameter/mm	Cylindricity/mm
1	0.5043	0.000589
2	0.5041	0.000776
7	0.5042	0.000782
8	0.5043	0.000598
11	0.5044	0.000772
13	0.5040	0.001212
16	0.5040	0.000707
17	0.5040	0.000935
24	0.5041	0.000798
26	0.5044	0.000764
28	0.5038	0.000697

The hole-plate sample (shone diagrammatically in Fig. 3) was manufactured and calibrated by the Physikalisch-Technische Bundesanstalt Braunschweig und Berlin (PTB) [45] (sample number "PTB 3" in [45]).

The sample is a stainless-steel plate measuring (6×6×1) mm with 28 holes with nominal diameter of 0.5 mm. The exact dimensions of the sample we use here were quantified by PTB and are summarised in Table 2.

2.2 X-ray CT scanner

All scans were carried out at the μ-VIS X-ray Imaging Centre at the University of Southampton, Southampton, United Kingdom. A Nikon/X-tek systems Ltd. custom-built X-ray CT scanner was used to perform the experiments. Image acquisition and overall control of the system was performed with the Nikon/X-tek systems Ltd. Inspect-X software (Inspect-X v2). A Nikon 450 kV micro-focus X-ray tube was used as a source, with a tungsten (W) reflection target for the step cylinder, whilst a Nikon 225 kV source was used for the hole plate. Both sources allow for exchangeable x-ray filters. The system also features an XYZ sample stage, and a high sensitivity flat panel detector (Perkin Elmer XRD 1621 CN3 EHS, with (2000×2000) pixels of 0.2 mm pixel pitch), movable linearly in three orthogonal directions.

At the detector, an analogue gain, measured in decibels (dB), is used to multiply the recorded signal (photon counts per pixel) to compute the output signal (grey value intensity stored as 16 bit unsigned integers). The system provides the capability of frame averaging, where projection images are taken repeatedly at the same rotation angle, which are then averaged, thus reducing photon counting and thermal noise.

A shuttling feature slightly shifts the detector over the duration of image acquisition with radiographs being co-registered post-imaging, a process that minimises errors originating in mechanical misalignment of the imaging setup. Both methods, frame averaging and shuttling, improve the imaging quality by suppressing imaging errors at the expense of longer scan times. Projection images can be taken either using a stop/start scanning approach, where the manipulator is rotated to a new angle, the motion stopped and only then, a projection image is taken. The alternative is to use a continuous rotation scanning approach, where a continuous rotation is used with images acquired whilst the object remains in motion. Continuous rotation is much faster, but will introduce increased blurring for longer exposure times or when averaging over more frames.

2.3 CT data acquisition

Two scans were performed for each of the two samples. Scan parameters are given in Table 3. One slow, high-quality scan used frame averaging, long exposure times and stop/start scanning, whilst a fast scan used short exposure times, no frame averaging and a continuous rotation scanning strategy. The slow scan minimised noise whilst the fast scan

minimised overall data acquisition time. Both scans took the same number of projection images to allow standard tomographic reconstruction.

Table 3: The scan parameters for the slow and fast scan.

	Slow scan	Fast scan	Low projection
Step cylinder			
CGLS			
Iterations	20	20	20
FISTA (TV)			
Iterations	20	75	75
Hyper	220000	6000	6000
TV iteration	20	20	20
Lambda	0.1	0.1	0.1
Hole plate			
CGLS			
Iterations	20	20	20
FISTA (TV)			
Iterations	20	20	20
Hyper	220000	220000	220000
TV iteration	100	100	100
Lambda	10	10	10

Table 4: The reconstruction protocols for the slow and fast scans of the step cylinder, for the CGLS algorithm and the FISTA TV algorithm.

	Step cylinder		Hole plate	
Scan speed	Slow	Fast	Slow	Fast
X-ray tube voltage/kV	390	390	120	120
X-ray tube curent/mA	0.245	0.216	0.083	0.083
Power/W	95.6	84.2	10	10
Exposure time/ms	708	250	134	134
Frames per projection	16	1	16	1
Number of projections	3143	3143	3143	3143
Filter sheet thickness/mm	8	8	-	-
Filter sheet material	Copper	Copper	-	-
Shuttling	Yes	No	Yes	No
Start/Stop or Continuous	S/S	Cont.	S/S	Cont.
Scan duration /mins	760	13	112	7

For the step cylinder the slow scan took 760 minutes, whilst the fast scan took 13 minutes (58 times faster). For the hole-plate the slow scan took 112 minutes, while the fast scan took 7 minutes (16 times faster). The temperature in the CT scanner was recorded as (25 ± 1) °C. Sample projection images for fast and slow scans are shown in Fig. 4 for both samples, with magnified image portions showing the image noise. The slow scan was then used to generate an additional dataset by discarding projections, thus simulating another fast scan, where this time few low noise projections are used.

Table 5: The reconstruction protocols for scans of the hole-plate sample and for increasing number of projections, for the CGLS algorithm and the FISTA TV algorithms.

No of projections	131	262	524	1028
CGLS				
Iterations	75	75	75	75
FISTA (TV)				
Iterations	75	75	75	75
Hyper	22	333	955	2200
TV iterations	100	100	100	100
Lambda	0.1	0.1	0.1	0.1

Table 6: The reconstruction protocols for scans of the hole-plate sample and for increasing Poisson noise variance, for the CGLS and the FISTA TV algorithms.

Photon count	1,800	18,000	90,000
CGLS			
Iterations	75	75	75
FISTA (TV)			
Iterations	75	75	75
Hyper	2200	2200	2200
TV iterations	100	100	100
Lambda	0.1	0.1	0.1

These low projection fast scans used only 54 projections to simulate a scan that, for the step-cylinder, would have been as fast as the high noise scan. These scans were used in a first experiment to compare the effects on dimensional metrology of the different approaches to increase imaging speed and the effects of different reconstruction algorithms on these.

In a second set of experiments, further simulated scans were produced from the low noise fast scans. The first set of simulated data used the low noise images, but reduced the dataset size to 132, 262, 524 and 1048 equally spaced projections, whilst a second set of simulated data added Poisson noise to the projections to simulate data that would have been acquired with 1,800, 18,000 and 90,000 photons per pixel along x-ray paths that do not intersect with the object (we also generated data with an average photon count of 180 photons per pixel, but this data did not provide reconstructions that allowed surface fitting).

2.4 Reconstruction

All data-sets (the slow, low noise reference scans, the high noise scans and the low number of projection scans) of the step-cylinder and the hole-plate samples were reconstructed using the standard Feldkamp-Davis-Kress (FDK) [23], [45] algorithm as implemented in the TIGRE tomographic reconstruction software [46] [29]. This FDK reconstruction was used as the baseline to compare the performance of two iterative methods. The FDK reconstruction of the slow, low noise scans were also used to calibrate the system parameters and to determine the size of the reconstructed voxels to match the average coordinate measurement machine dimensions for both samples. This allowed us to analyse the performance of alternative reconstruction algorithms, such as the CGLS [30]; [31] [32], and FISTA-TV algorithms [33], both implemented in the TIGRE toolbox [46] [29].

Parameters for the iterative algorithms for the first set of experiments, where we reconstructed the slow, low noise data, the fast, high noise data and the low noise data with only 54 projections are shown in Table 4. FISTA-TV algorithm parameters were optimised by running a few iterations of the reconstruction over a grid of parameters and observing image quality. Example reconstruction images are shown in Fig. 5 where we show slices through the reconstruction volume of the step cylinder sample, dissecting
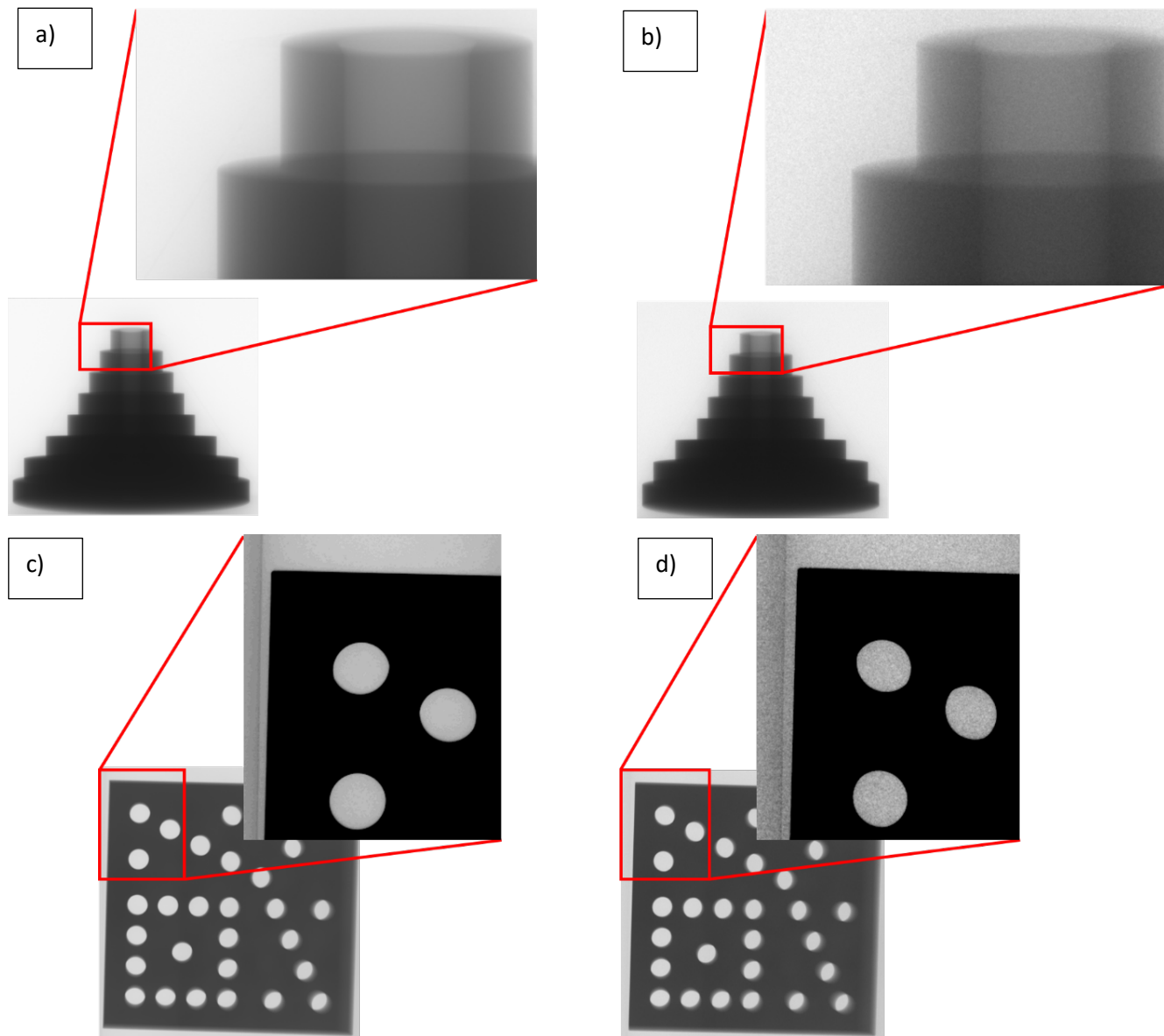

Figure 4: Sample radiographs of the cylinder-stack (a, b) and the hole-plate (c, d) samples, with a detail in the red box enlarged for better preview. Slow scan radiographs in (a) and (c) comprise higher SNR compared to their fast scan equivalents (b) and (d), respectively.
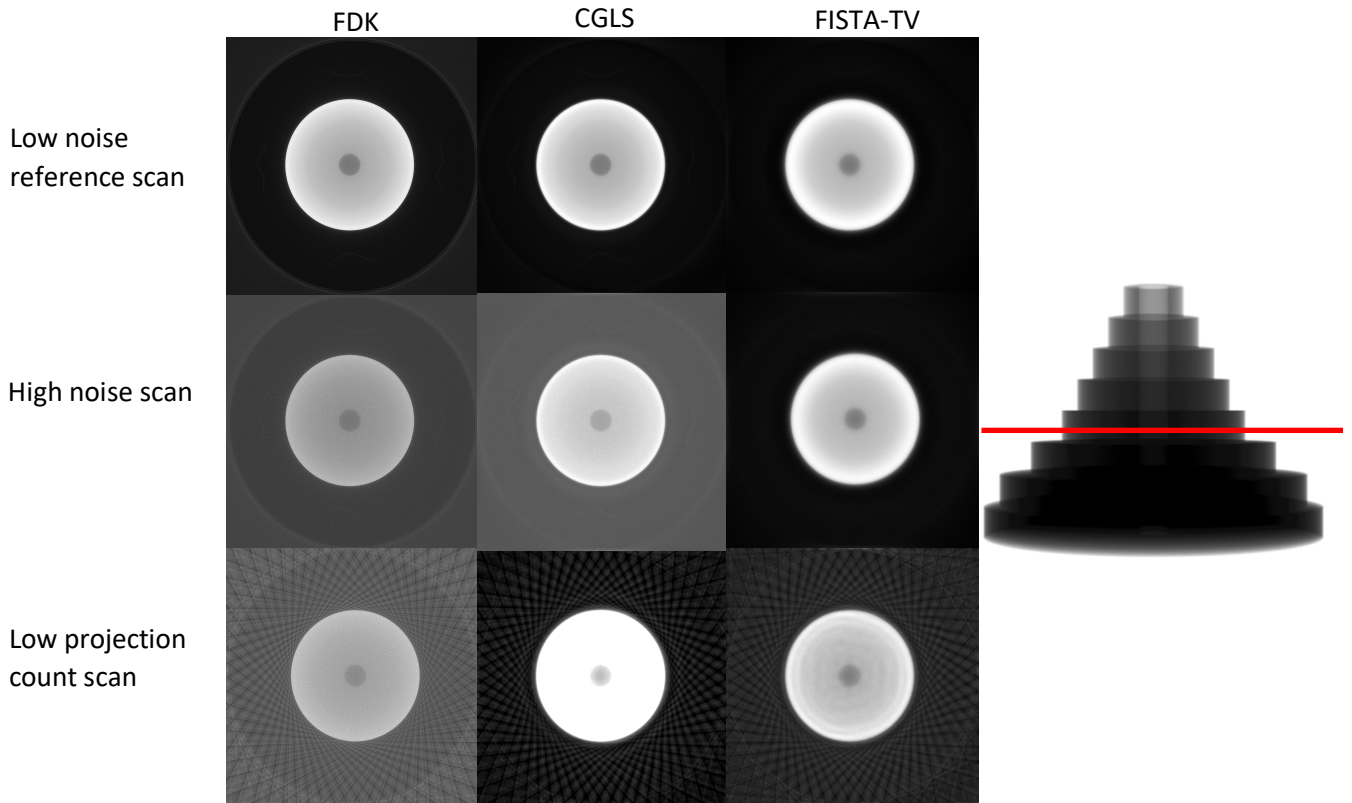
Figure 5: Comparison of scan settings and reconstruction methods in an image slice passing through step 4.

the fourth step from the bottom and Fig 6., where we show portion of a slice through the centre of the reconstructed hole plate. The parameters for the iterative algorithms for the second set of experiments, where we reconstructed the 4 data sets with different projection counts and the three datasets with different noise levels, were tuned in a similar way. The parameters are shown in Table 5 and Table 6.

2.5 Surface determination and measurements

For the first experiment, surface determination was carried out using VG studio 3.4 using the advanced mode iterative surface determination method provided in the VG Metrology package. For the step cylinder, the cylinder axis of the smallest diameter step was used to define a co-ordinate axis (We initially planned to use the internal through hole as axis to define the coordinate system, but beam hardening artefacts prevented the fitting of a cylinder to this feature). We then defined orthogonal planes relative to that axis, where each plane intersected the centre of each cylindrical step. The intersection of the step boundary and the relevant plane defined measurement points to which a circle was fitted. We then measured the root mean square deviation of measurement points from the circle as well as the max/min deviation.

For the hole plate, we again used VG studio 3.4 using the advanced mode iterative surface determination method to fit

all surfaces. We used the front surface to define a reference plane. We then fit cylinders to all holes, using holes 1 and 6 to define a coordinate axis by connecting the intersections of the two cylinder central axes and the reference surface. Using the normal to the surface as another axis then provided an orthogonal co-ordinate system for measurement. We measured the diameters of all cylinders as well as centre to centre distances (measured on the reference surface) for cylinder hole pairs (1,28), (6,20), (26,20), (1,26), (1,6), (4,27) and (14,19).
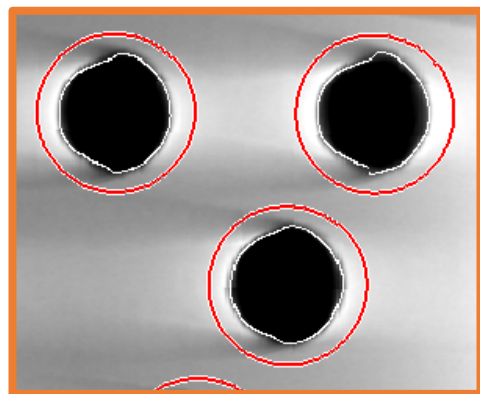

Figure 6: Circles (red) derived using the Huff transform identify the location of each hole. Canny edge detection identifies hole boundaries (white). Circle fitting (not shown) fits circles to identified boundary points.
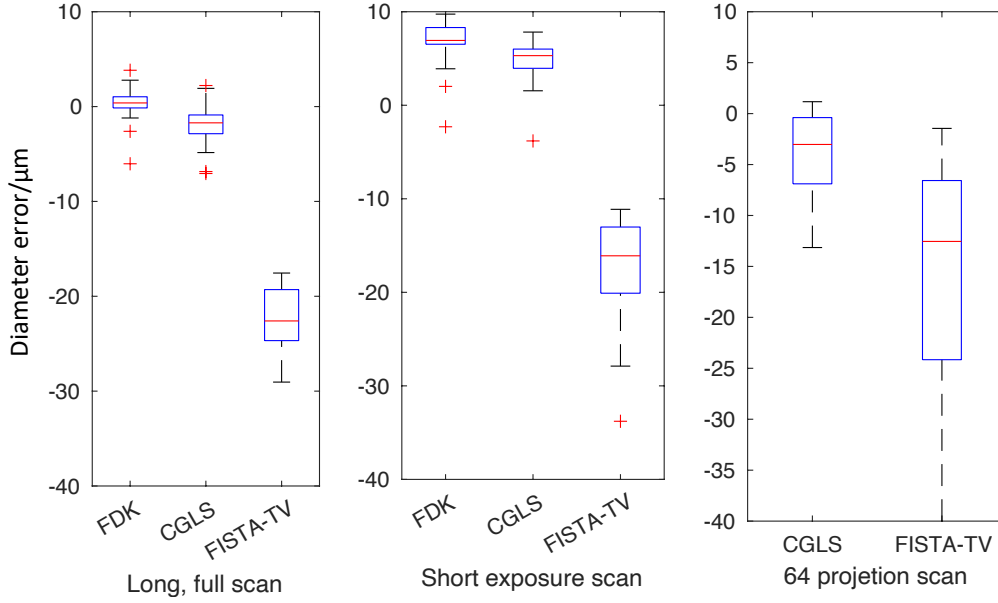
Figure 7: Box and whisker plots of the errors in the hole diameter estimates in μm for the hole plate for the different measurements (low noise scan (right), high noise scan (middle) and low number of projection scan (right)) for the three different algorithms. Box and whisker plots show the median (red line), interquartile range from 25 % to 75 % percentile points (blue box), the -3 standard deviations (std) to +3 std from the data mean range (black whiskers) and outliers (red +), i.e., points > 3 std and < -3 std.

For all measurements, the CMM data for sample features was then used as a baseline to estimate the systematic error [2] $E = x_{CT} - x_{ref}$ and relative errors: $E_r = \frac{x_{CT} - x_{ref}}{x_{ref}}$, where x_{ref} is the reference measurement [47] [48].

For the second set of experiments, we analysed only the data from the hole plate. As it is unclear what procedure VG studio's iterative surface determination approach takes and to verify our results using an alternative approach, Canny edge detection was used to determine object surfaces. The central line between top and bottom surface points was identified and the three dimensional data was resampled along the central slice using bi-cubic interpolation to produce a two dimensional image. The Huff circle finding method was used to locate all holes and generate masks for hole location including both the hole and a margin around the hole. Canny edge detection identified hole boundaries in each masked area (see Fig. 6). A least squares approach was used to fit a circle to the boundary points of each hole. Circle diameters and hole centre to centre distances were computed for all holes and hole pairs. Looking at Fig. 6 we also see visible distortion of the detected holes, which were here mainly due to beam hardening artefacts [45] evidence of which can be seen here, which was further verified using the full reconstructed volume (not shown).

3. Results and discussion

Results for the errors in the measurement of outer diameters (step cylinder) with the different algorithms is shown in Fig. 7, where we show the error in the measured diameters for each method and each of the three datasets plotted against the nominal diameters of each cylinder. It is worth noting that for larger diameters, beam-hardening effects become evident.

Results for the errors in measuring inner diameters (hole plate data) with the different algorithms is shown in Fig. 8, where we show a box whisker plot for the errors for all holes for any one dataset/algorithm combination.

Fig. 9 quantifies the average error as well as the standard deviation of the errors in the hole plate. We here look at the inner diameter error and its variation for 26 all holes as well as the average relative error and its variation for hole centre to centre distances between hole pairs (6-20), (20-26), (4-27), (1-26), (14-19), (1-6) and (1-28). For the outer diameters of the step cylinder, we see that the error for all methods varies with step diameter and this is here likely to be due to beam hardening effects, with larger steps showing increasing beam hardening issues in the reconstruction due to the highly attenuating material used (aluminium). Another observation is that both, the CGLS and the FISTA method give biased results, with the bias being positive for the outer diameters (outer diameters are overestimated) whilst the inner diameters lead to negative bias (inner diameters are
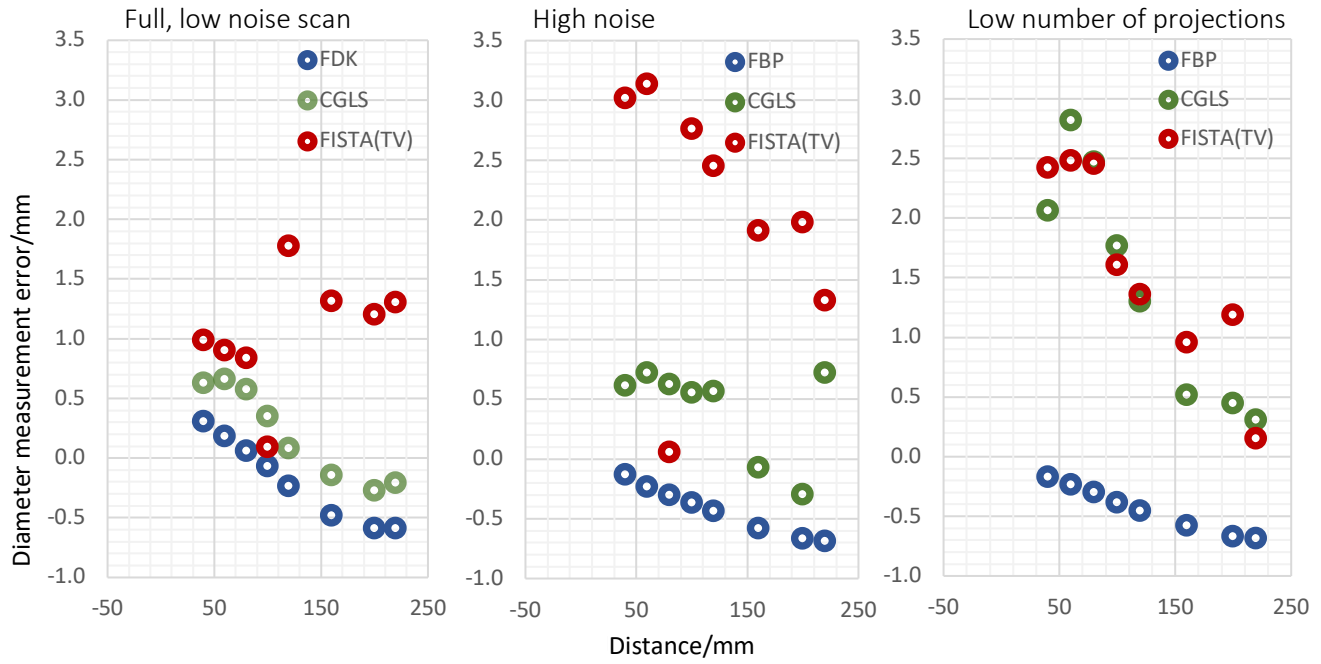
Figure 8: Measurement errors for the measurements of outer diameters measured on the step cylinder from the slow, low noise scan for the FISTA(TV) algorithm, the CGLS algorithm and the FDK algorithm.

underestimated). Crucially, the bias is much larger for the FISTA-TV method, indicating that the Total Variation constraint leads to boundary estimates that are biased towards the outside of the object. Note that this is similar to issues known to be produced in XCT based surface

determination, where inner diameters tend to be more sensitive to image noise and artefacts [49] and our results suggests that this issue is further amplified by the use of the TV constraint in the reconstruction.
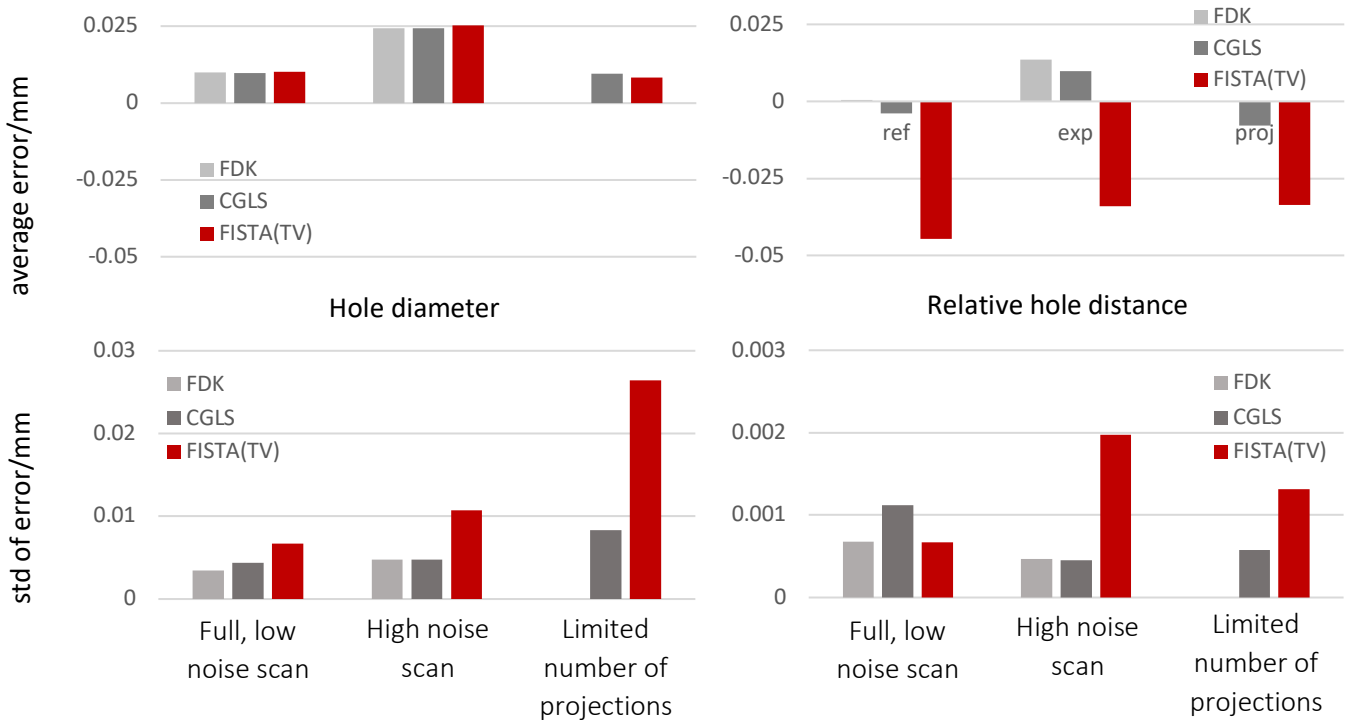

Figure 9: Average (top) and standard deviation (bottom) in the error in the hole diameter (left) and the relative hole centre to centre distance (right) for the three hole plate datasets for all three algorithms. FDK did not provide reliable surface estimates for the limited projection data.
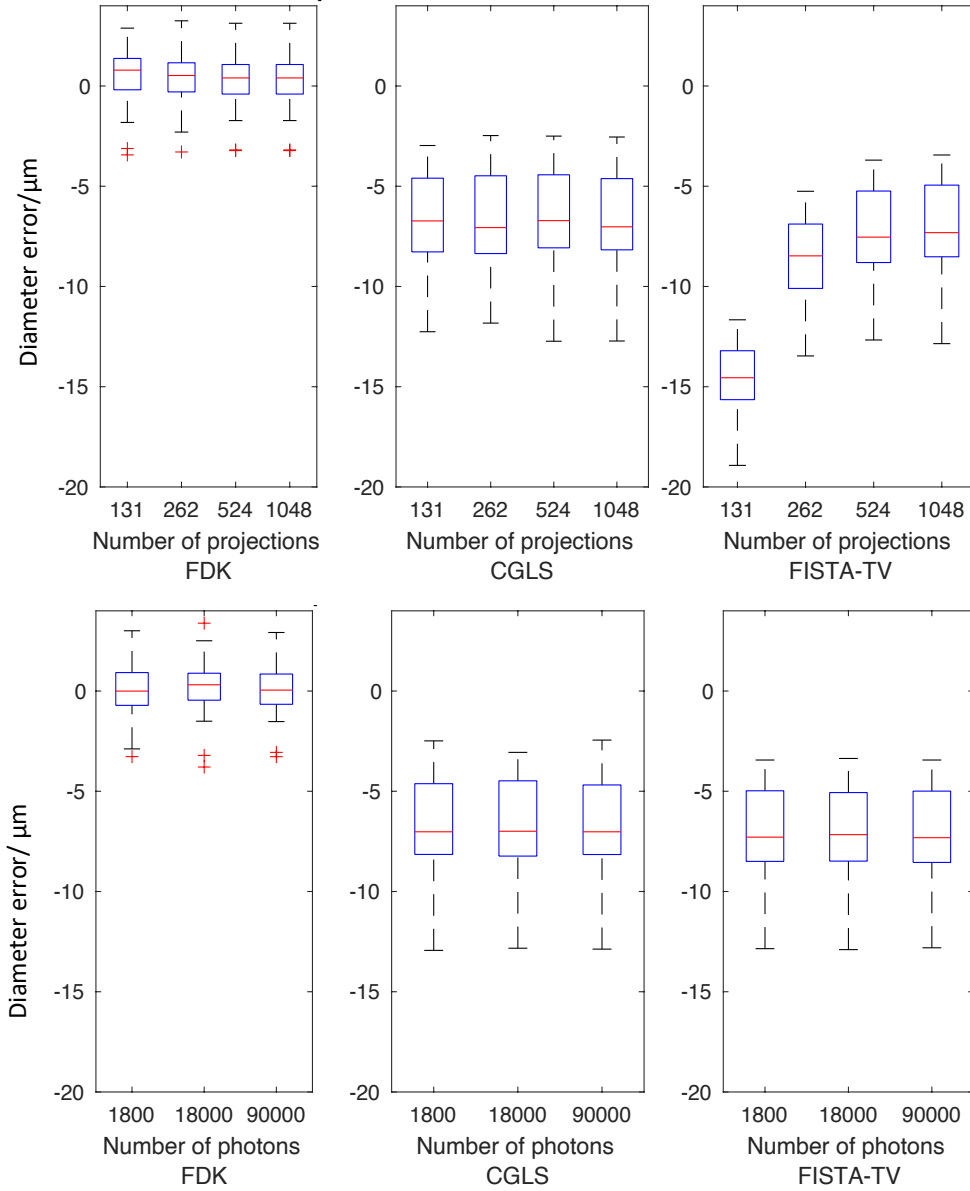
Figure 10: Box and whisker plots of the hole diameter errors (in μm) measured for the hole plate using limited numbers of x-ray photons (top) and limited numbers of projections (bottom) and reconstructed with the three different algorithms.

Another observation is that the results for the FISTA algorithm show much larger variation compared to the other methods. This is particularly evident for steps 5 and 6 of the phantom, where the FDK reconstruction provides significantly different results for the three data-sets. Note that the FDK algorithm was not able to reconstruct the hole plate low projection count data with sufficient accuracy to allow us to fit the required surfaces, so results for this case are missing here.

To analyse the influence of the surface fitting used and to see the performance of the methods over a wider range of noise levels and reductions in projections, we used the artificially generated noisy scan data and a wider range of the low

projection count data as described above. Results are shown in Figure 10, where we show the errors in the hole diameter estimates achieved with the different methods. Again, we see that the CGLS method and the FISTA-TV algorithm led to increasingly biased results, with the bias in the FISTA-TV reconstruction getting worse in for the dataset with the smallest numbers of projections, mirroring the results above. The same deterioration is not shown in the FISTA results for the data with the highest noise level. Note, that, when reconstructing the data using a photon count of 180, we did not find reliable edges to use our circle fitting approach. We see that the results for the FISTA algorithm here show smaller errors compared to those found for the results with the low noise data. This indicates that either, the slightly
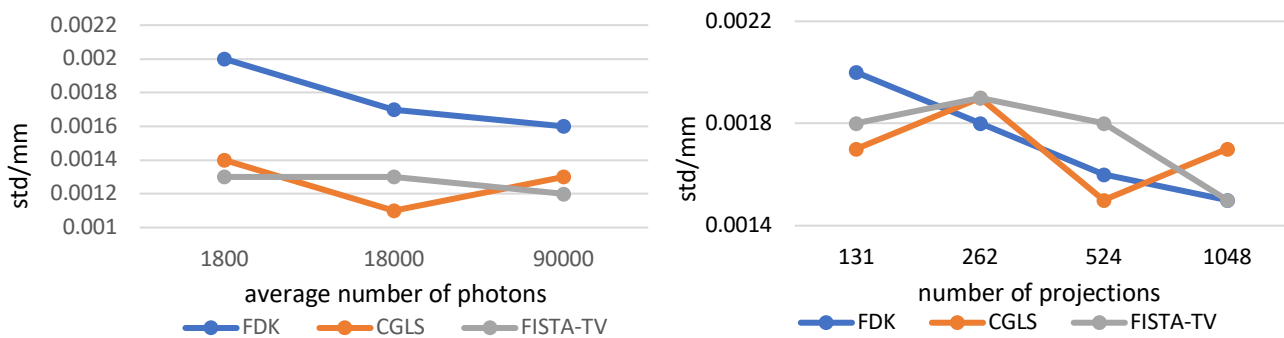
Figure 11: The standard deviation of the normalised distance between through holes on the hole plate in mm plotted for the three algorithms for different numbers of photon counts per pixel (left) and different number of projections (right).

different FISTA-TV parameter choice used here gives rise to somewhat different results or that the surface determination approach used above is more sensitive to the FISTA-TV bias than the Canny method.

These results suggest that both surface determination methods are relatively robust to the photon counting noise associated with acquisitions with shorter exposure times, whilst the streaking artefacts introduced when reducing the numbers of projections more quickly deteriorates surface estimates. Whilst the centre-to-centre hole distance measures are more robust than the hole diameter estimates (which is to be expected as biases in surface estimation here cancel out), looking at the standard deviation of the normalised error in hole to hole distances across the sample shows an increase in distance measure variability for all methods and for both scenarios for the increase of noise and the decrease in the number of projections (Fig 11). This change is relatively predictable for the FDK reconstruction, which, for example, shows a near linear decrease in the standard deviation of the normalised distance error for doubling numbers of projection. For CGLS and in particular the FISTA-TV results, this relationship is less clear with results much more variable.

4. Conclusion

We have here shown how a reduction in scan time can be achieved in XCT metrological measurements by decreasing x-ray exposure or by reducing the number of x-ray projections. Whilst iterative algorithms can help with the loss of fidelity, results also become increasingly biased and more variable depending on the type and amount of image degradation induced by the faster imaging strategy.

In particular, we observed that a total variation based reconstruction method biased surfaces to be located further towards the outside of the objects, making inner diameter measures smaller and outer measures larger, a phenomenon

previously observed in dimensional XCT, but here shown to be stronger with TV based reconstruction, but also observed, though to a lower extent, for the least squares approach. For example, FISTA-TV reconstruction led to a median relative error in the estimation of inner diameters of -2.8% (with 131 projections, a 24 times speedup) to -1.4% (with 1048 projections, a 3 times speed up) relative to FDK reconstruction. The standard deviation in the error increased by approximately 25 % for all of these conditions with FISTA-TV. For 64 projections, the standard deviation in the relative measurement error for FISTA-TV increased from 0.5 % to 1.3 % though here, FDK reconstruction no longer provided usable surface estimates. Similar, but opposite effects were observed for the outer diameters, with the FISTA-TV reconstruction leading to a median relative error in the estimation of outer diameters of -2.1 % (with 64 projections, a 49 times speedup) relative to FDK reconstruction with a standard deviation in the relative error of 2.1 % compared to a standard deviation of only 0.03 % for the FDK algorithm.

Comparing the decrease in x-ray exposure to the reduction of the number of projections, we observe a doubling in the error standard deviation for the inner diameter measurements when going from the reduced exposure time scans and the limited projection scans for both iterative methods, whilst the FDK method completely fails for the limited projection data. For the outer diameter, the same trend is observed, though it is here more variable.

Acknowledgements

authors acknowledge the μ-VIS x-ray imaging centre at the University of Southampton for the provision of the x-ray tomographic imaging facilities.

References

[1]   I. Puertas, C. Luis Pérez, D. Salcedo, J. León, R. Luri and J. Fuertes, "Precision study of a coordinate measuring machine using several contact probes," *Procedia Engineering,* vol. 63, pp. 547-555, 2013.

[2]   H. Villarraga-Gómez, C. Lee and S.T. Smith, "Dimensional metrology with X-ray CT: A comparison with CMM measurements on internal features and compliant structures," *Precision Engineering,* vol. 51, pp. 291-307, 2018.

[3]   S. Lou, S. Brown, W. Sun, W. Zeng, X. Jiang and P. Scott, "An Investigation of the Mechanical Filtering Effect of Tactile CMM in the Measurement of Additively Manufactured Parts," *Measurement,* vol. 144, pp. 173-182, 2019.

[4]   E. Bos, "Aspects of tactile probing on the micro scale," *Precision Engineering,* vol. 35, no. 2, pp. 228-240, 2011.

[5]   P. Swornowski, "A critical look at the coordinate measuring technique," *Mechatronics,* vol. 23, no. 1, pp. 80-93, 2013.

[6]   H. Villarraga-Gómez, E.L. Herzo, and S.T. Smith, "X-ray Computed Tomography: From Medical Imaging to Dimensional Metrology," *Precision Engineering*, Vol. 60, pp. 544–569, 2019.

[7]   L. De Chiffre, S. Carmignato, J.-P. Kruth, R. Schmitt and A. Weckenmann, "Industrial applications of computed tomography," *CIRP Annals,* vol. 63, no. 2, pp. 655-677, 2014.

[8]   H. Villarraga-Gómez, "Seeing is believing: X-ray computed tomography for quality control," *Quality,* vol. 55, no. 6, p. 21, 2016.

[9]   A. Thompson and I. L. R. Maskery, "X-ray computed tomography for additive manufacturing: a review," *Measurement Science and Technology,* vol. 27, no. 7, p. 072001, 2016.

[10]   S. Everton, M. Hirsch, P. Stravroulakis, R. Leach and A. Clare, "Review of in-situ process monitoring and in-situ metrology for metal additive manufacturing," *Materials & Design,* vol. 95, pp. 431-445, 2016.

[11]   J. Stopp, R. Christoph and R. Christoph, "Production-Integrated Metrology with Modern Coordinate Measuring Machines Using Multisensor and X-Ray Computed Tomography Systems.," in *in The International Symposium for Production Research*, 2018.

[12]   M. Eberhorn, S. Oeckl, T. Stocker and F. Brunner, "Novel handling concept for production integrated computed tomography," in *World Congress on NDT*, 2016.

[13]   O. Brunke, F. Hansen, I. Stuke, F. Butz and F. Jeltsch, "A new Concept for High-Speed atline and inline CT for up to 100% Mass Production Process Control," in *16th International Congress of Metrology.*, 2013.

[14]   B. Gapinski, M. Wieczorovski, L. Marciniak-Podsadna, B. Dybala and G. Ziolkowski, "Comparison of different method of measurement geometry using CMM, optical scanner and computed tomography 3D," *Procedia Engineering,* vol. 69, pp. 255-262, 2014.

[15]   S. Carmignato and E. Savio, "Traceable volume measurements using coordinate measuring systems," *CIRP Annals,* vol. 60, no. 1, pp. 519-522, 2011.

[16]   R. Jiménez, S. Ontiveros, S. Carmignato and J. Yagüe, "Correction strategies for the use of a conventional micro-CT cone beam machine for metrology applications," *Procedia CIRP,* vol. 2, pp. 34-37, 2012.

[17]   F. Léonard, S. Brown, P. Withers, M. P. Mummery and M. McCarthy, "A new method of performance verification for x-ray computed tomography measurements.," *Measurement Science and Technology,* vol. 25, no. 6, p. 065401, 2014.

[18]   S. Carmignato, W. Dewulf and R. Leach, Industrial X-ray computed tomography, Springer, 2018.

[19]   J. Kruth, M. Bartscher, S. Carmignato, R. Schmitt, L. De Chiffre and A. Weckenmann, "Computed tomography for dimensional metrology," *CIRP Annals,* vol. 60, no. 2, pp. 821-842, 2011.

[20]   D. Xu, F. Cheng, Y. Zhou, T. Matalaray, P. Lim and L. Zhao, "Process optimization: internal feature measurement for additive-manufacturing parts using x-ray computed tomography," in *International Symposium on Precision Engineering Measurements and Instrumentation*, 2019.

[21]   Y. Quinsat, J. Guyon and C. Lartigue, "Qualification of CT data for areal surface texture analysis," *The International Journal of Advanced Manufacturing Technology,* vol. 100, no. 9-12, pp. 3025-3035, 2019.

[22]   W. Sun, C. Giusca, S. Lou X. Yanga, X. Chena, T. Fry, X. Jiang, A. Wilson S. Brown and H. Boulter, "Establishment of X-ray computed tomography traceability for additively manufactured surface texture evaluation," *Additive Manufacturing,* vol. 50, 2022.

[23]   L. Feldkamp, L. Davis and J. Kress, "Practical cone-beam algorithm," *JOSA A,* vol. 1, no. 6, pp. 612-619, 1984.

[24]   M. Shammaa, Y. Ohtake and H. Suzuki, "Segmentation of multi-material CT data of mechanical parts for extracting boundary surfaces," *Computer-Aided Design,* vol. 42, no. 2, pp. 118-128, 2010.

[25]   J. Lifton, A. Malcolm, J. McBride and J. Cross, "The application of voxel size correction in X-ray Computed Tomography for dimensional metrology," in *Singapore international NDT conference & exhibition*, 2013.

[26]   A. Kak and M. Slaney, Principles of computerized tomographic imaging, IEEE press, 1988.

[27]   X. Pan, E. Sidky and M. Vannier, "Why do commercial CT scanners still employ traditional, filtered back-projection for image reconstruction?" *Inverse problems,* vol. 25, no. 12, p. 123009, 2009.

[28]   N. Rezvani, Iterative reconstruction algorithms for polyenergetic x-ray computerized tomography., Canada: University of Montreal, 2012.

[29] A. Biguri, R. Lindroos, R. Bryll, H. Towsyfyan, H. Deyhle, I. Harrane, R. Boardman, M. Mavrogordato, M. Dosanjh, S. Hancock and T. Blumensath, "Arbitrarily large tomography with iterative algorithms on multiple GPUs using the TIGRE toolbox," *Journal of Parallel and Distributed Computing,* vol. 146, pp. 52-63, 2020.

[30] M. Hestenes and E. Stiefel, "Methods of Conjugate Gradients for Solving Linear Systems," *Journal of Research of the National Bureau of Standards,* vol. 49, no. 6, p. 409, 1952.

[31] C. Schorr, L. Dörr, M. Maisl and T. Schuster, "Registration of a priori information for computed laminography," *NDT & E International,* vol. 86, pp. 106-112, 2017.

[32] L. Helfen, A. Myagotin, P. Mikulík, P. Pernot, A. Voropaev, M. Elyyan, M. Di Michiel, J. Baruchel and T. Baumbach, "On the implementation of computed laminography using synchrotron radiation," *Review of Scientific Instruments,* vol. 82, no. 6, p. 063702, 2011.

[33] A. Beck and M. Teboulle, "A fast iterative shrinkage-thresholding algorithm for linear inverse problems," *SIAM journal on imaging sciences,* vol. 2, no. 1, pp. 183-202, 2009.

[34] L. Rudin, O. S. and E. Fatemi, "Nonlinear total variation based noise removal algorithms," *Physica D,* vol. 60, p. 259–268, 1992.

[35] H. Lettenbauer, A. Lotze and S. Kunzmann, "Method and device for identifying material boundaries of a test object". Patent US20080089589A1, 2011.

[36] F. Welkenhuyzen, Y. Tan, K. Kiekens, W. Frank, T. Ye, B. Philip, V. André, D. Wim, K. Jean-Pierre, P. Bleys, W. Dewulf, J. Kruth, A. Voet and K. Kim, "A test object for calibration and accuracy assessment in X-ray CT metrology," in *IMEKO 10th Int. Symp. on Measurement and Quality Control*, 2010.

[37] G. Kerckhofs, J. Schrooten, M. Wevers, P. Van Marcke and T. Van Cleynenbreugel, "Standardisation and Validation of Micro-CT for the Morphological Characterisation of Porous Structures," in *9th Eur. Conf. Non-Destructive Testing (ECNDT),* Berlin, Germany. 2006.

[38] J. Hiller, M. Maisl and L. Reindl, "Physical characterization and performance evaluation of an x-ray micro-computed tomography system for dimensional metrology applications," *Measurement Science and Technology,* vol. 23, no. 8, p. 085404, 2012.

[39] H. Villarraga-Gómez, "X-ray computed tomography for dimensional measurements," in *Digital Imaging*, 2016.

[40] A. Kraemer and G. Lanza, "Assessment of the measurement procedure for dimensional metrology with X-ray computed tomography," *Procedia CIRP,* vol. 43, pp. 362-367, 2016.

[41] F. Welkenhuyzen, K. Kiekens, M. Pierlet, W. Dewulf, P. Bleys, J. Kruth and A. Voet, "Industrial computer tomography for dimensional metrology: Overview of influence factors and improvement strategies," in *4th International Conference on Optical Measurement Techniques for Structures and Systems (OPTIMESS)*, 2009.

[42] J. Warnett, V. Titarenko, E. Kiraci, A. Attridge, W. Lionheart, P. Withers and M.A. Williams, "Towards in-process x-ray CT for dimensional metrology," *Measurement Science and Technology,* vol. 27, no. 3, p. 035401, 2016.

[43] H. Villarraga-Gómez & S.T. Smith in "Effect of the number of projections on dimensional measurements with X-ray computed tomography", *Precision Engineering,* vol 66, pp. 445-456, 2020.

[44] P. Schuetz, I. Jerjen, J. Hoffmann, M. Plamondon, A. Flisch and U. Sennhauser, "Reducing the influence of environmental scattering in industrial computed tomography by system optimisation and correction algorithms," in *11th European Conference on Non-Destructive Testing (ECNDT)*, 2014.

[45] M. Bartscher, J. Illemann and U. Neuschaefer-Rube, "ISO test survey on material influence in dimensional computed tomography," *Case Studies in Nondestructive Testing and Evaluation,* vol. 6, no. B, pp. 79-92, 2016.

[46] A. Biguri, M. Dosanjh, H. S. and S. M., "TIGRE: a MATLAB-GPU toolbox for CBCT image reconstruction," *Biomedical Physics & Engineering Express,* vol. 2, no. 5, p. 055010, 2016.

[47] JCGM, "Evaluation of measurement data—Guide to the expression of uncertainty in measurement," Int. Organ. Stand, Geneva, 2008.

[48] L. Mari, "The problem of foundations of measurement," *Measurement,* vol. 38, no. 4, pp. 259-266, 2005.

[49] H. Villarraga-Gómez, L. Körner, R. Leach, S.T. Smith, "Amplitude-wavelength maps for X-ray computed tomography systems," *Precision Engineering*, vol. 64, pp. 228-242, 2020.